Intraseasonal Periodicity in the Southern Hemisphere Circulation on Regional Spatial Scales

DAVID W. J. THOMPSON, BRIAN R. CROW, AND ELIZABETH A. BARNES

Department of Atmospheric Science, Colorado State University, Fort Collins, Colorado

(Manuscript received 24 March 2016, in final form 6 December 2016)

ABSTRACT

Wave activity in the Southern Hemisphere extratropical atmosphere exhibits robust periodicity on time scales of ~20–25 days. Previous studies have demonstrated the robustness of the periodicity in hemispheric averages of various eddy quantities. Here the authors explore the signature of the periodicity on regional spatial scales.

Intraseasonal periodicity in the Southern Hemisphere circulation derives from out-of-phase anomalies in wave activity that form in association with extratropical wave packets as they propagate to the east. In the upper troposphere, the out-of-phase anomalies in wave activity form not along the path of extratropical wave packets, but in their wake. The out-of-phase anomalies in wave activity give rise to periodicity not only on hemispheric scales, but also on synoptic scales when the circulation is sampled along an eastward path between ~5 and 15 m s^{-1}. It is argued that 1) periodicity in extratropical wave activity derives from two-way interactions between the heat fluxes and baroclinicity in the lower troposphere and 2) the unique longitude–time structure of the periodicity in upper-tropospheric wave activity derives from the contrasting eastward speeds of the source of the periodicity in the lower troposphere (~10 m s^{-1}) and wave packets in the upper troposphere (~25 m s^{-1}).

1. Introduction

Hemispheric-scale variability in the Southern Hemisphere (SH) extratropical circulation can be viewed in the context of two distinct structures, both of which exhibit a high degree of zonal symmetry: 1) the southern annular mode (SAM; Kidson 1988; Hartmann and Lo 1998; Thompson and Wallace 2000) and 2) its baroclinic counterpart, the baroclinic annular mode (BAM; Thompson and Woodworth 2014).

The two patterns have very different signatures in the extratropical flow. The SAM emerges as the leading empirical orthogonal function (EOF) of zonal-mean kinetic energy, is characterized by north–south shifts in the extratropical jet, and is associated with large variations in the eddy fluxes of momentum (Hartmann and Lo 1998; Thompson and Wallace 2000). In contrast, the BAM emerges as the leading EOF of the eddy kinetic energy, is characterized by a hemispheric-scale monopole in extratropical wave amplitudes, and is associated with large variations in the eddy fluxes of heat (Thompson and Woodworth 2014). The differences between the structures also extend to their time variations. As is the case for most large-scale patterns of extratropical variability, the SAM can be modeled as Gaussian red noise with a decorrelation time scale of ~10 days (Hartmann and Lo 1998; Feldstein 2003). Interestingly, the power spectrum of the BAM is not consistent with Gaussian red noise but, rather, exhibits robust periodic variability on time scales of ~25 days (Thompson and Woodworth 2014; Thompson and Barnes 2014).

The periodicity associated with the BAM has potentially important implications for understanding intraseasonal climate variability on hemispheric scales: it is readily apparent in hemispheric means of extratropical eddy kinetic energy, the eddy fluxes of heat, precipitation, and longwave cloud radiative effects (Thompson and Barnes 2014; Li and Thompson 2016). However, to what extent the periodicity is apparent in regional-scale variations in the flow—and thus its potential implications for regional weather—remains unclear.

The purpose of this study is to explore the periodicity in the BAM on regional spatial scales. To do so, we will revisit the ''downstream development'' of synoptic-scale

Corresponding author e-mail: David W. J. Thompson, davet@atmos.colostate.edu

DOI: 10.1175/JAS-D-16-0094.1

disturbances (e.g., Simmons and Hoskins 1979; Lee and Held 1993; Chang 1993; Chang and Yu 1999; Chang 1999, 2005). The results support the central findings of previous observational analyses of downstream development—namely, that wave packets in the extratropical upper troposphere propagate to the east at a rate close to the speed of the zonal flow in the upper troposphere. But the results also highlight a novel aspect of extratropical disturbances not documented in previous work: as wave packets propagate eastward and decay in the upper troposphere, they are accompanied by opposite-signed anomalies in eddy kinetic energy that form to the west of the decaying wave packet. The opposite-signed anomalies give rise to periodicity on not only on hemispheric scales but also on regional scales when the circulation is sampled along eastward paths between ~5 and 15 m s^{-1}.

Section 2 provides details on the data and methods. Section 3 explores the periodicity in SH eddy kinetic energy in the context of individual wave packets. In section 4 we 1) develop a simple model of the interactions between the extratropical baroclinicity, eddy fluxes of heat, and eddy kinetic energy and 2) use the model to provide a physical interpretation of the observations. Concluding remarks are provided in section 5.

2. Data and methods

The observational analyses are based on four-times-daily-resolution values of the European Centre for Medium-Range Weather Forecasts interim reanalysis dataset (ERA-Interim; Dee et al. 2011). The reanalyses data were processed on a 1.5° × 1.5° grid and for the period 1 January 1979–31 December 2015 (a total of 13 514 days). All observational results are based on analyses of anomalous data for all calendar days of the year, where anomalies are formed by 1) calculating the long-term average of the data as a function of calendar day and 2) subtracting the resulting seasonal cycle from the data as a function of grid box and vertical level.

Eddy kinetic energy is defined as $(u^{*2} + v^{*2})/2$, where the asterisk denotes departures from the zonal mean. The eddy kinetic energy is first calculated at 4-times-daily resolution and then averaged over 24-h periods to form daily mean values.

The BAM index time series is defined as the leading principal component (PC) time series of EKE calculated over all levels and latitudes within the domain 1000–200 hPa and 20°–70°S. The data are weighted by the square root of the cosine of latitude and the mass represented by each vertical level before calculating the PC time series.

Power spectra are found by the following steps: 1) calculating the spectra for subsets of the data that are 500 days in length (all subsets are treated with a Hanning window and have an overlap with adjacent subsets of 250 days); 2) averaging the subset power spectra over all subsets; and 3) applying a five-point running mean to the resulting mean power spectrum. Independent spectral estimates in the resulting mean spectrum have roughly 270 degrees of freedom. The statistical significance of spectral peaks (i.e., Fig. 6) is found by applying the F statistic to the ratio of the amplitude of individual spectral peaks to a red-noise fit of the time series. The red-noise fit is estimated from the lag-1 autocorrelation of the time series. Spectra are shown in units of cycles per day (cpd).

The significance of the results in the longitude–time lag regression plot (i.e., Fig. 3) is estimated by applying a two-tailed test of the t statistic to the corresponding correlation coefficients. The effective number of degrees of freedom for the significance test is estimated as

$$n_{\text{eff}} = n\frac{1 - r_{1x}r_{1y}}{1 + r_{1x}r_{1y}},$$

where n is the number of timesteps, r_{1x} and r_{1y} are the lag-1 autocorrelations of the time series being correlated (typically ~0.25 for the eddy kinetic energy time series used in the analysis), and n_{eff} is the effective number of degrees of freedom. As discussed in section 3, the results shown in the longitude–time lag regression plots (e.g., Fig. 3) are averages of regression coefficients calculated for all 240 base longitudes in the analysis. To be conservative, we did not increase n_{eff} to account for averaging results over multiple base longitudes, even though the averaging increases the number of degrees of freedom in the analysis.

In many analyses here, the eddy fields are analyzed as a function of longitude. Since the eddy fields are defined as departures from the zonal mean, the variance of the eddy component of the circulation at any given longitude includes—by construction—a component of the variance of the circulation at other longitudes. In practice, the zonal mean makes only a small contribution to the total variance in the circulation on grid point scales. For example, the correlation coefficients r between v and v^* at the 700-hPa level are greater than 0.99 at all longitudes along 50°S.

3. Observed periodicity in extratropical eddy kinetic energy

The structure and time-dependent behavior of the BAM are reviewed briefly in Fig. 1. The left panel shows the structure of the BAM in the anomalous eddy kinetic energy at 300 hPa; the right panel shows the power spectrum of the associated BAM index time series. The

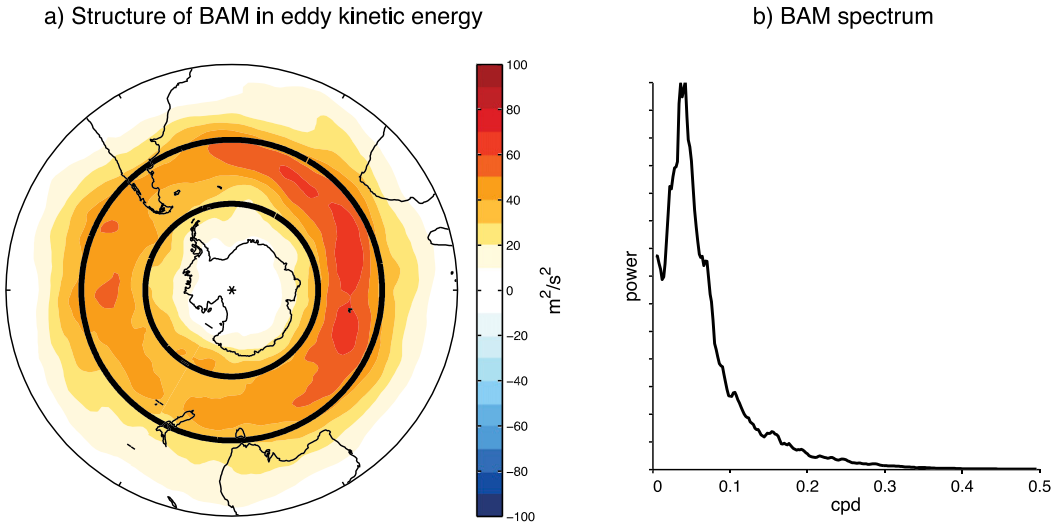

FIG. 1. (a) Eddy kinetic energy anomalies at 300 hPa regressed onto the BAM index time series, defined as the leading PC time series of eddy kinetic energy over all levels and latitudes within the domain 1000–200 hPa and 20°–70°S. Solid thick black lines indicate latitude circles at 40° and 60°S. (b) Power spectrum of the BAM index time series (cpd). See text for details.

spatial structure of the BAM is marked by hemispheric-scale fluctuations in eddy kinetic energy that span much of the SH storm track within the latitude band roughly 40°–60°S (Thompson and Woodworth 2014). Its time-dependent behavior is dominated by a broad spectral peak on time scales of roughly 25 days (right panel; Thompson and Woodworth 2014). As noted in the introduction, the periodicity in the BAM is readily apparent in SH-mean eddy kinetic energy. In this section, we will explore its signature on regional spatial scales.

Figure 2 examines the spectrum of SH eddy kinetic energy on increasingly smaller zonal scales. The results are generated as follows. First, we average eddy kinetic energy over the latitude band 40°–60°S, which corresponds to the approximate meridional span of the storm track and thus of the BAM (Fig. 1, left; 40° and 60°S are indicated by the solid thick black circles). The resulting data matrix (herein $EKE_{40°–60°S}$) is resolved as a function of time and longitude. Next, we calculate the power spectrum of $EKE_{40°–60°S}$ over various zonal scales: all longitudes (Fig. 1a) and longitudinal windows of width 180° (Fig. 1b), 90° (Fig. 1c), and 30° (Fig. 1d). Note that the power spectra in Figs. 1b–d are found by averaging power spectra calculated for all possible windows of the indicated width (e.g., in the case of Fig. 1b, spectra are calculated and averaged over the longitudinal windows 1.5°E–178.5°W, 3°E–177°W, . . . , 180°–0°).

The power spectrum of zonal-mean $EKE_{40°–60°S}$ (Fig. 2a) exhibits robust periodicity on time scales of ~25 days and is very similar to the power spectrum of the BAM (Fig. 1b; Thompson and Woodworth 2014) and upper-tropospheric eddy kinetic energy averaged over the entire SH (Thompson and Barnes 2014). The spectrum of $EKE_{40°–60°S}$ averaged over 180° longitudinal windows (Fig. 2b) also exhibits enhanced power centered about ~25 days, but the amplitude of the peak is diminished relative to the zonal-mean case. The amplitude of the peak is further diminished when the width of the longitudinal window is reduced to 90°. The peak in the spectrum is largely imperceptible when the zonal scale is reduced to 30° (~8000 km; Fig. 2d).

Why is the spectral peak in zonal-mean eddy kinetic energy so weak on spatial scales less than ~180°? To address this question, we generate a composite longitude–time lag regression plot for eddy kinetic energy in the SH storm track region. The plot is formed as follows: 1) $EKE_{40°–60°S}$ at all longitudes is regressed onto standardized values of $EKE_{40°–60°S}$ at base longitude λ for time lags ranging from −30 to +30 days, 2) step 1 is repeated for all base longitudes $0° < \lambda < 360°$, and 3) the resulting individual regression plots are averaged to form a composite longitude–time lag regression plot averaged over all base longitudes. Note that the general features highlighted in the composite regression plot are found in individual regression plots based on a single base longitude but that averaging the regression plots over all base longitudes increases the sample size of the analysis.

The resulting longitude–time lag regression plot is shown in the left panel of Fig. 3. Note that 1) the lowest contour values correspond to regression coefficients that are significant at the 95% confidence level (see section 2)

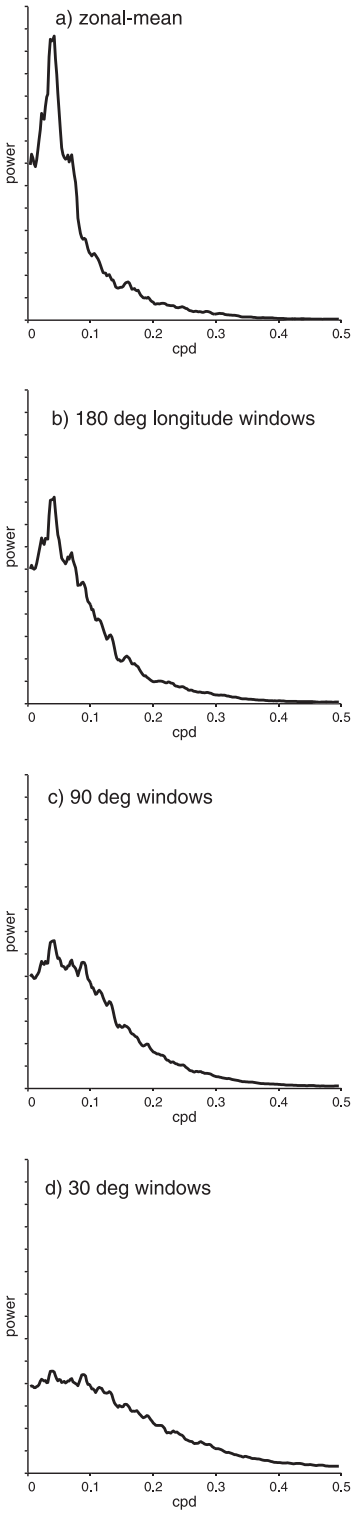

FIG. 2. Power spectra of eddy kinetic energy anomalies at 300 hPa averaged over 40°–60°S: (a) zonal mean and (b)–(d) averages over longitude bands of indicated widths. See text for details.

and 2) the symmetry of results at positive and negative lags is a property of the autocorrelation function. The primary features in the time–longitude evolution of $EKE_{40°–60°S}$ have been documented extensively in previous analyses of the downstream development of wave packets in numerical models (Simmons and Hoskins 1979), Northern Hemisphere storm tracks (Chang 1993; Chang and Yu 1999), and SH storm tracks (Lee and Held 1993; Chang 1999, 2005). The results confirm two widely established aspects of disturbances in the extratropical storm tracks: 1) individual disturbances in EKE propagate to the east at a rate similar to flow speeds in the lower troposphere (roughly $8\,m\,s^{-1}$ in Fig. 3, left) whereas 2) the envelope of successive disturbances in EKE propagates to the east at a rate close to the speed of the zonal flow in the upper troposphere (roughly $25\,m\,s^{-1}$ in Fig. 3, left). However, the results also reveal a novel aspect of SH extratropical disturbances that has not been highlighted in previous work: a band of negative EKE anomalies that form to the west of the original wave packet as it propagates eastward. The negative anomalies in EKE are very weak but are statistically significant at the 95% level based on a two-tailed test of the t statistic (see section 2). As discussed later, the negative anomalies in EKE play a central role in driving the periodicity in the flow on hemispheric scales.

The right panel in Fig. 3 shows the corresponding regression coefficients for zonal-mean $EKE_{40°–60°S}$. Interestingly, the negative regression coefficients begin to develop somewhat earlier on regional scales (left panel) than they do in the zonal mean (right panel). The reasons for this distinction can be gleaned from the longitudinal structure of the wave packet. When the negative regional-scale regression coefficients first develop, they are smaller than the positive coefficients associated with the decaying wave packet that lies to the east. The negative coefficients only project onto the zonal mean after the original wave packet has largely decayed, after about day 8.

Figures 4 and 5 provide an alternative view of the longitude–time lag regression plot of SH eddy kinetic energy. The results are identical to those shown in the left panel of Fig. 3 but for two differences: 1) we have applied a 30°-longitude running mean to the regression coefficients to visually enhance the downstream development of the wave packet relative to the phase of individual eddies (the spatial smoothing was not applied to Fig. 3) and 2) we have displayed the results as a series of filled line plots. Figure 4 shows the regression coefficients out to lag +12 days. Figure 5 focuses on results at positive lag and shows coefficients out to lag +30 days. Note that in both figures 1) the base longitude of the

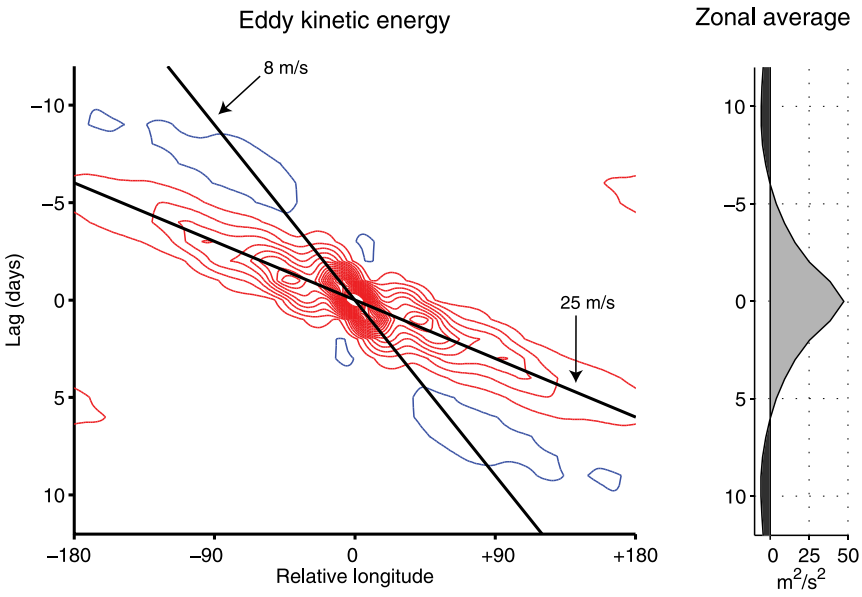

FIG. 3. (left) Longitude–time lag regression plot for eddy kinetic energy anomalies at 300 hPa averaged over 40°–60°S ($EKE_{40°–60°S}$). Results are found by averaging longitude–time regression plots formed for all base longitudes. Longitude 0° indicates the base longitude of the analysis. The lowest contour value corresponds to regression coefficients that are significant at the 95% level (see section 2). Contours at −3.25, +3.25, 9.75 $m^2 s^{-2}$, ... Blue contours denote negative values, and red contours indicate positive values. (right) Corresponding lag regressions for zonal-mean $EKE_{40°–60°S}$.

analysis is denoted by relative longitude 0° and 2) the results are repeated in longitude so that the anomalies can be traced as they wrap around the globe. The associated zonal-mean regression coefficients are shown in the right panels of both figures.

The results in Figs. 4 and 5 visually enhance the negative EKE anomalies that develop to the west of the original wave packet as it decays. The negative anomalies develop around shortly after lag 0, propagate eastward in the lee of the original wave packet, peak around day +7, and decay by around day +20. The negative anomalies in EKE are followed by a new packet of positive anomalies in EKE that have largest amplitude around 25 days after the peak in the original wave packet (Fig. 5). The positive anomalies at lags greater than ~20 days are relatively weak but nevertheless give rise to significant positive regression coefficients in the zonal mean (Fig. 5, right panel).

The unique time–longitude pattern of successive positive and negative EKE anomalies highlighted in Figs. 4 and 5 is important for two reasons: 1) it gives rise to robust periodicity in the spectrum of zonal-mean EKE (Fig. 2), and 2) it leads to weak but significant periodicity in power spectra of regional-scale EKE following the flow, as shown next.

Figure 6 shows the power spectra of $EKE_{40°–60°S}$ following the flow at rates ranging from 0 to 25 $m\,s^{-1}$. For each rate, the spectra are 1) calculated separately for all starting zonal grid boxes and then 2) averaged over all starting grid boxes. For example, the spectra at 10 $m\,s^{-1}$ is found by 1) rearranging the $EKE_{40°–60°S}$ data matrix so that the first day in the matrix corresponds to $EKE_{40°–60°S}$ at zonal grid box i, the second day to $EKE_{40°–60°S}$ at zonal grid box $i + \Delta i$, where Δi corresponds to the number of grid boxes traveled in 1 day at 10 $m\,s^{-1}$, etc., 2) calculating the power spectrum of the resulting data matrix for all starting zonal grid boxes, and 3) averaging the resulting power spectra. The black circles on the contour plot indicate the frequency of maximum spectral power for cases where the spectral peak is statistically different from the red-noise fit at the 95% level (section 2). The black vertical line indicates the frequency of maximum spectral power for zonal-mean $EKE_{40°–60°S}$ (i.e., the maximum in the spectrum shown in Fig. 2a).

As indicated in Fig. 6, the power spectrum of $EKE_{40°–60°S}$ does not exhibit coherent periodicity at a fixed longitude (i.e., at a rate of 0 $m\,s^{-1}$). The power spectrum also does not indicate coherent periodicity following the flow at a rate comparable to the wave packet (~25 $m\,s^{-1}$). Rather, the power spectrum of $EKE_{40°–60°S}$ only exhibits significant periodicity on the scale of individual grid boxes at flow speeds between ~5 and 15 $m\,s^{-1}$. The reasons for this are visually apparent in Figs. 4 and 5.

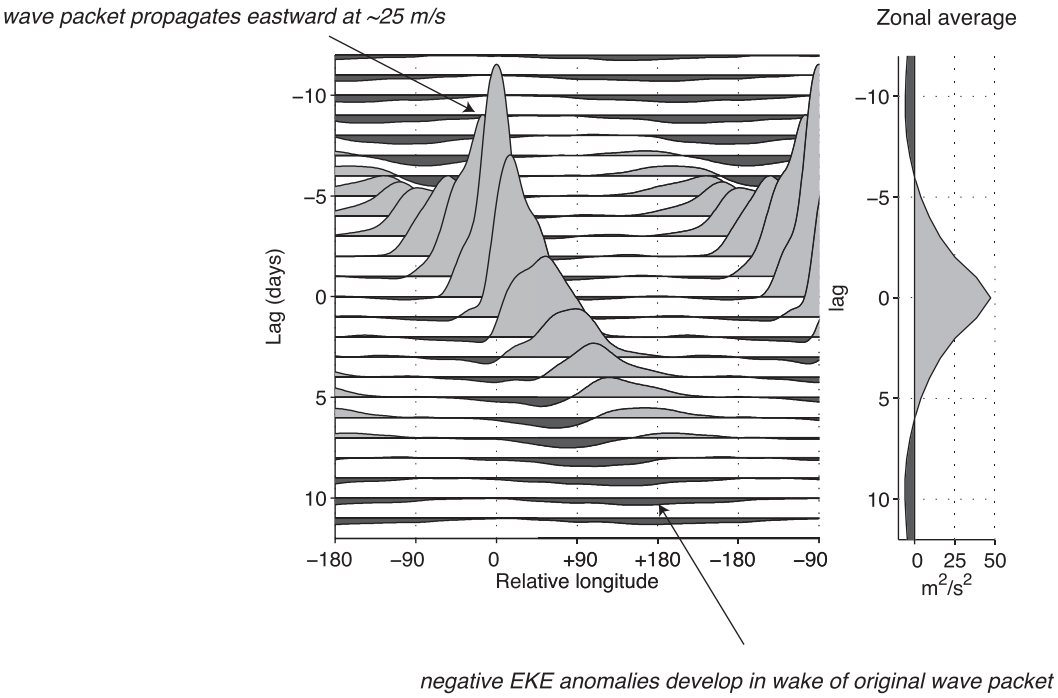

FIG. 4. (left) As in Fig. 3, but results are smoothed with a 30°-longitude running-mean filter and are shown as a series of filled line plots. Note the longitude axis is extended relative to Fig. 3 so that the anomalies can be traced as they wrap around the globe. The largest amplitude is ~100 $m^2 s^{-2}$ at lag 0. (right) Corresponding lag regressions for zonal-mean $EKE_{40°–60°S}$.

The negative EKE anomalies that peak around lag +7 days do not evolve at a fixed longitude. Nor do they emerge along the path of the wave packet. Rather, they emerge in the wake of the wave packet as it propagates to the east. Importantly, the largest amplitudes in the spectra occur at frequencies comparable to the frequency of maximum spectral power for zonal-mean $EKE_{40°–60°S}$ (roughly 0.04 cpd) regardless of the eastward rate used to sample the flow.

In the following section, we provide a physical interpretation of the unique time–longitude pattern of the alternating positive and negative EKE anomalies associated with SH wave packets.

4. Physical interpretation

In Thompson and Barnes (2014) we argued that the periodicity in SH-mean eddy kinetic energy arises from two-way interactions between the baroclinicity and eddy fluxes of heat in the lower troposphere. The argument is based on two physical relationships: 1) from baroclinic instability theory, periods of anomalously high baroclinicity lead to anomalously poleward eddy fluxes of heat, and vice versa, and 2) from the thermodynamic energy equation, periods of anomalously poleward eddy fluxes of heat lead to decreases in baroclinicity, and vice versa. Similar feedbacks between the baroclinicity and baroclinic wave activity underlie early theories of the "zonal-index cycle" (Rossby and Willett 1948) and more recent analyses of periodic behavior in the North Atlantic storm track (Ambaum and Novak 2014; Novak et al. 2015).

The observed relationships between the baroclinicity and eddy fluxes of heat in the Southern Hemisphere were quantified in Thompson and Barnes (2014) for the zonal-mean circulation. The observed relationships are probed for the zonally varying circulation in the top panel of Fig. 7. The top panel in Fig. 7 shows the time series of the lower-tropospheric (700 hPa) eddy fluxes of heat averaged 40°–60°S (herein $vT_{40°–60°S}$) regressed as a function of lag and relative longitude onto standardized values of $vT_{40°–60°S}$ at a base longitude. The figure is generated in an identical manner to Fig. 3 but for two differences: 1) the results are based on the eddy fluxes of heat, not eddy kinetic energy; and 2) the regression coefficients are smoothed with a 30°-longitude running-mean filter to emphasize the behavior of the wave packet relative to the phase of individual eddies. The coefficients are multiplied by −1 so that the primary center of action centered about lag 0 days indicates anomalously poleward (negative) heat fluxes.

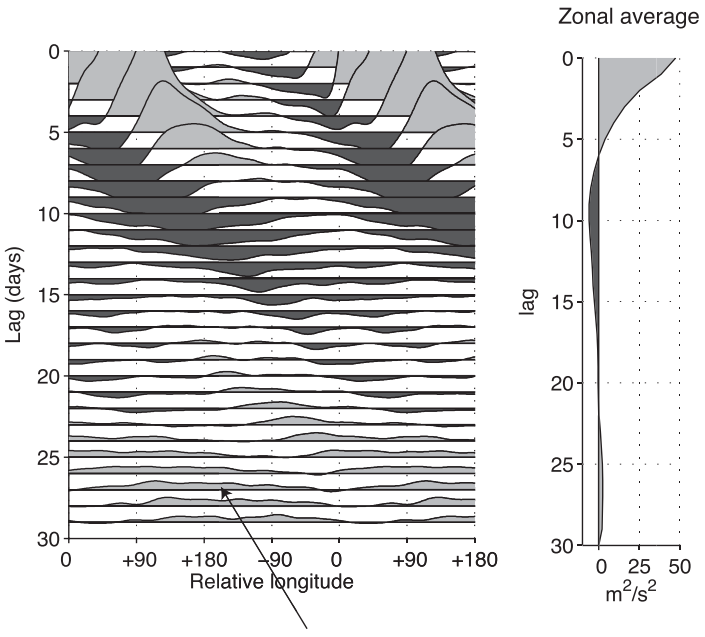

FIG. 5. As in Fig. 4, but for lags extending from 0 to +30 days. Note the longitude axis in the left panel is shifted to the east of that in Fig. 4 so that the anomalies can be traced as they wrap around the globe.

By construction, the anomalous eddy fluxes of heat have largest amplitude at a time lag 0 days and relative longitude of 0° (Fig. 7, top). The poleward anomalies in $vT_{40°–60°S}$ at lag 0 days are accompanied by two sets of out-of-phase anomalies. The most prominent set includes positive anomalies in $vT_{40°–60°S}$ that form along the 25 m s^{-1} isotach at a lag of ~1–2 days. The out-of-phase anomalies along the 25 m s^{-1} isotach give rise to periodicity on time scales of ~2–3 days in power spectra of $vT_{40°–60°S}$ following the flow to the east at ~25 m s^{-1} (not shown). They reflect vacillations in the phase of the eddies and do not contribute to periodicity in the wave packet on weekly time scales.

The second set of out-of-phase anomalies includes positive anomalies in $vT_{40°–60°S}$ that form along the 8 m s^{-1} isotach at lags beyond ~5 days. The out-of-phase anomalies centered along the 8 m s^{-1} isotach are only apparent in the longitude–time lag regression plot for $vT_{40°–60°S}$ when the contour interval is reduced by a factor of ~5 (result not shown), but this saturates the regression coefficients elsewhere on the figure. Nevertheless, the positive anomalies in $vT_{40°–60°S}$ beyond ~5 days are statistically significant and—importantly—give rise to a broad peak in the spectrum of zonal-mean $vT_{40°–60°S}$ centered between ~15 and 25 days (Fig. 8, dashed line). The peak in the spectrum of zonal-mean $vT_{40°–60°S}$ is similar but not identical to that found in association with zonal-mean $EKE_{40°–60°S}$ (solid line; reproduced from Fig. 2a). The spectrum for zonal-mean $EKE_{40°–60°S}$ has largest amplitude centered about 25 days and very little power at higher frequencies; in contrast, the spectrum for zonal-mean $vT_{40°–60°S}$ has 1) a relatively broad spectral peak that spans periods between ~15 and 25 days and 2) substantial power at higher frequencies. As discussed further below, the contrasts between the spectra in Fig. 8 suggest that the periodicity in $EKE_{40°–60°S}$ reflects the damped harmonic response to periodicity in $vT_{40°–60°S}$.

The middle panel of Fig. 7 indicates the lower-tropospheric baroclinicity anomalies that occur in conjunction with the heat flux anomalies in the top panel. The results are generated by 1) calculating the meridional temperature gradient at 700 hPa averaged over 40°–60°S (hereafter denoted $b_{40°–60°S}$) and 2) regressing the resulting baroclinicity anomalies onto standardized values of $vT_{40°–60°S}$ as a function of longitude and lag. (In principal, the baroclinicity is the ratio of the meridional and vertical gradients in temperature; in practice, variations in the static stability play a secondary role in determining the results of the analysis). Positive anomalies denote increases in the equator-to-pole temperature gradient, and vice versa. Consistent with results shown for the zonal-mean circulation in Thompson and Barnes (2014), periods of anomalously poleward heat fluxes

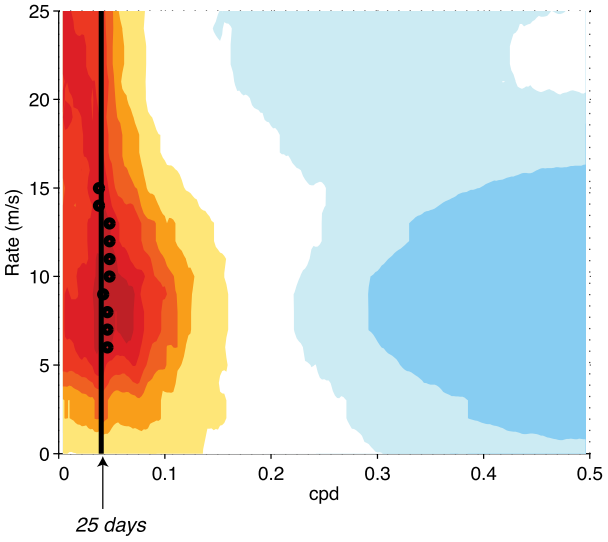

FIG. 6. Power spectra of $EKE_{40°–60°S}$ following the flow eastward at indicated rates. Circles denote the frequency of maximum power for each eastward rate for cases where the spectral peak is statistically different from the red-noise fit at the 95% level. The vertical black line denotes the frequency of maximum power for the spectrum of zonal-mean eddy kinetic energy (0.04 cpd or 25 days). All spectra are normalized to unit variance. See text for details of the analysis.

(top panel) are preceded by periods of anomalously high baroclinicity (middle panel, red contours) and followed by periods of anomalously low baroclinicity (middle panel, blue contours). The periodic variability in lower-tropospheric baroclinicity is transported eastward along the ~8 m s^{-1} isotach (Fig. 7, middle), consistent with the behavior of the heat fluxes discussed above.

The bottom panel in Fig. 7 indicates the corresponding relationships between the lower-tropospheric eddy fluxes of heat and upper-tropospheric eddy kinetic energy. In this case, the results show $EKE_{40°–60°S}$ as a function of relative longitude and lag regressed on standardized values of $vT_{40°–60°S}$. Consistent with the energetics of baroclinic waves (e.g., Simmons and Hoskins 1978), periods of anomalously poleward lower-tropospheric heat fluxes (top panel) precede periods of anomalously high upper-tropospheric eddy kinetic energy (bottom panel). In contrast to the relationships between the eddy fluxes of heat and the baroclinicity, the linkages between the eddy fluxes of heat and the eddy kinetic energy are primarily one way: that is, variations in the lower-tropospheric eddy fluxes of heat lead variations in upper-tropospheric eddy kinetic energy but do not clearly follow them. The variations in $EKE_{40°–60°S}$ propagate to the east at roughly 25 m s^{-1}, consistent with the propagation of upper-tropospheric eddy kinetic energy anomalies evidenced in Figs. 3–5, but notably faster than the propagation of the ~15–25-day signal in the

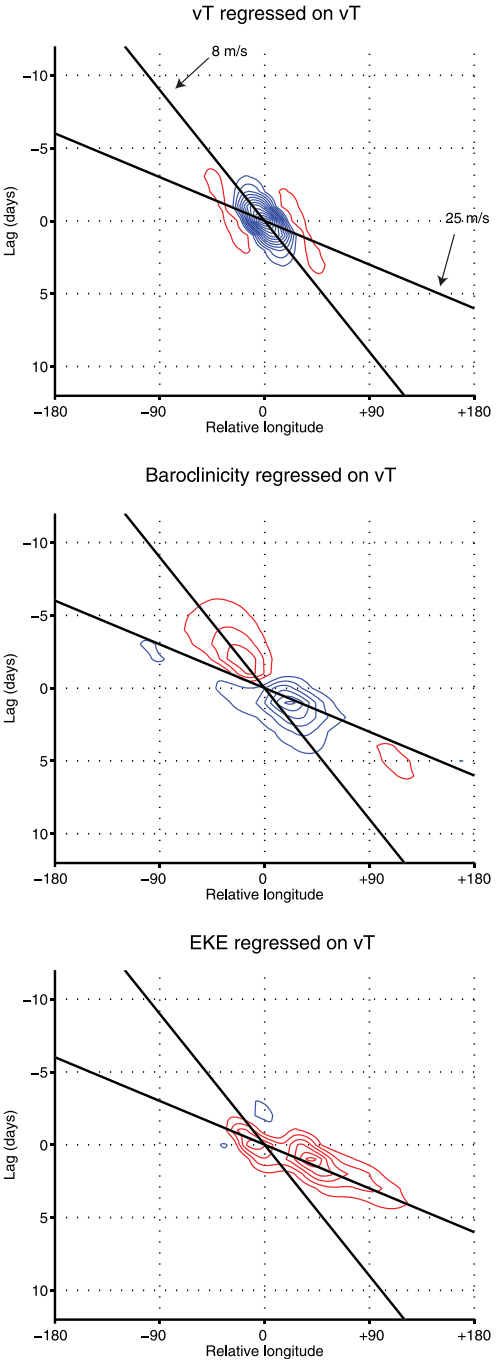

FIG. 7. Longitude–time lag regression plots based on the time series of the eddy heat flux anomalies at 700-hPa averaged over 40°–60°S latitude ($vT_{40°–60°S}$). (top) $vT_{40°–60°S}$ regressed on the $vT_{40°–60°S}$ time series as a function of lag and longitude. Negative values (blue contours) denote anomalously poleward eddy heat flux anomalies. (middle) The baroclinicity averaged over 40°–60°S regressed on the $vT_{40°–60°S}$ time series as a function of lag and longitude. (bottom) $EKE_{40°–60°S}$ regressed on the $vT_{40°–60°S}$ time series as a function of lag and longitude. Results are smoothed with 30°-longitude running-mean filter to emphasize the behavior of the wave packet relative to the phase of individual eddies. Contours are indicated at (top) −0.5, 0.5, 1.5 K m s^{-1}, . . .; (middle) −0.03, +0.03, 0.09 K (1000 km)$^{-1}$, . . .; and (bottom) −3.25, +3.25, 9.75 m^2 s^{-2}, ...

lower-tropospheric baroclinicity and heat fluxes, as discussed above.

In the next subsections, we develop and explore a simple model of the feedbacks between the baroclinicity, eddy fluxes of heat, and eddy kinetic energy in the SH storm track motivated by the observations in Fig. 7. The model is analogous to that developed in Thompson and Barnes (2014) but for two primary differences: 1) it is not zonally symmetric and thus includes zonal advection of the baroclinicity and propagation of eddy activity and 2) it includes equations for both the eddy fluxes of heat and eddy kinetic energy.

a. Developing the simple model

The model includes three equations: 1) a prognostic equation for the baroclinicity in the lower troposphere, 2) a prognostic equation of the eddy fluxes of heat in the lower troposphere, and 3) a prognostic equation for eddy activity in the upper troposphere. All equations are averaged over the meridional scale of the SH storm-track region (assumed here to be 40°–60°S) but are not averaged zonally. Hence the model includes zonal but not meridional advection and propagation.

The prognostic equation for baroclinicity is derived from the thermodynamic energy equation and is predicated on two assumptions. First, we assume that the eddy fluxes of heat are diffusive so that the time rate of change of the baroclinicity can be modeled as linearly proportional to the amplitude of the heat fluxes. Second, we assume that the damping of the baroclinicity by both adiabatic and diabatic processes can be modeled as linear damping. Applying both assumptions to the thermodynamic energy equation and linearizing about a basic state with time-mean, zonal-mean flow U_{lower} yields

$$\frac{\partial}{\partial t}b_{40°–60°S} + U_{\text{lower}}\frac{\partial}{\partial x}b_{40°–60°S} = \alpha_b \upsilon T_{40°–60°S} - \frac{b_{40°–60°S}}{\tau_b}, \quad (1)$$

where $b_{40°–60°S}$ and $\upsilon T_{40°–60°S}$ denote the anomalous baroclinicity and eddy fluxes of heat, respectively, in the lower troposphere averaged meridionally over the band 40°–60°S (recall that the baroclinicity is estimated as the meridional temperature gradient); $U_{\text{lower}}(\partial/\partial x)b_{40°–60°S}$ denotes the eastward advection of the anomalous baroclinicity by the climatological-mean, zonal-mean lower-tropospheric flow; α_b is a linear regression coefficient analogous to the eddy diffusivity; and τ_b is the damping time scale of the baroclinicity.

The prognostic equation for the eddy fluxes of heat is derived from the Eady growth rate and is based on three assumptions. First, we assume that the growth rate of baroclinic waves in the lower troposphere—and thus their heat fluxes—is linearly proportional to the baroclinicity. The assumption follows from baroclinic instability theory and the Eady growth rate (e.g., Lindzen and Farrell 1980; Hoskins and Valdes 1990). Second, we assume that the sink of the heat fluxes (due to Rossby wave radiation and breaking) is well modeled as linear damping. Third, we assume that baroclinic wave activity in the lower troposphere propagates eastward at a rate comparable to the time-mean, zonal-mean flow in the lower troposphere. As such, the time rate of change of the anomalous heat fluxes is approximated as

$$\frac{\partial}{\partial t}\upsilon T_{40°–60°S} + U_{\text{lower}}\frac{\partial}{\partial x}\upsilon T_{40°–60°S} = \alpha_{\upsilon T} b_{40–60°S} - \frac{\upsilon T_{40°–60°S}}{\tau_{\upsilon T}}, \quad (2)$$

where $U_{\text{lower}}(\partial/\partial x)\upsilon T_{40°–60°S}$ denotes the eastward propagation of the anomalous heat fluxes associated with eddy activity, $\alpha_{\upsilon T}$ is a linear regression coefficient derived from the observed relationships between the baroclinicity and the wave fluxes of heat (discussed below), and $\tau_{\upsilon T}$ is the damping time scale for the eddy fluxes of heat.

Note that in Eqs. (1) and (2), the baroclinicity and heat fluxes both propagate eastward at the same rate (U_{lower}). In reality, they are not constrained to do so: the baroclinicity propagates eastward relative to surface wind as a baroclinic surface Rossby wave; the heat fluxes are advected eastward at a rate comparable to the steering level of individual waves. Nevertheless, in practice, the observed eastward propagation rates for

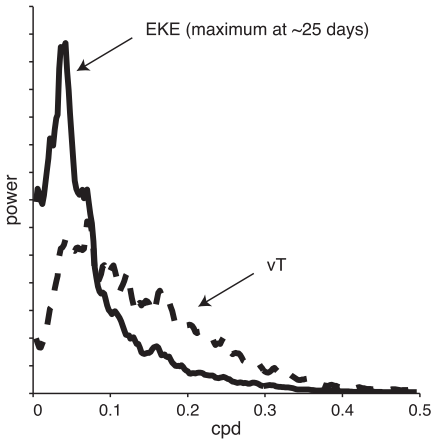

FIG. 8. Power spectra showing a reproduction of the zonal-mean eddy kinetic energy anomalies at 300 hPa averaged over 40°–60°S latitude from Fig. 2a (solid) and the zonal-mean eddy heat flux anomalies at 700 hPa (dashed). Spectra are normalized to unit variance.

both fields are very similar: the lag–longitude autoregression plots for the heat fluxes (top panel of Fig. 7) and baroclinicity (not shown) at 700 hPa are both marked by primary centers of action that propagate to the east at roughly $\sim 8\,\mathrm{m\,s^{-1}}$.

The prognostic equation for the eddy kinetic energy in the upper troposphere is motivated by the eddy kinetic energy equation (e.g., Chang 1993) and the energetics of baroclinic waves (Simmons and Hoskins 1978). It is predicated on three main assumptions. First, we assume that the horizontal and vertical eddy fluxes of heat are closely linked in baroclinic systems and, thus, that the baroclinic conversion of eddy potential to eddy kinetic energy is linearly related to the anomalous eddy fluxes of heat. Second, we assume that the sinks of eddy kinetic energy are well modeled as linear damping. Third, we assume that wave activity in the upper troposphere propagates eastward at a rate comparable to the time-mean, zonal-mean flow in the upper troposphere. Applying the above assumptions to the EKE equation yields the following expression for the time rate of change of the anomalous eddy kinetic energy:

$$\frac{\partial}{\partial t}\mathrm{EKE}_{40^\circ\text{–}60^\circ\mathrm{S}} + U_{\mathrm{upper}}\frac{\partial}{\partial x}\mathrm{EKE}_{40^\circ\text{–}60^\circ\mathrm{S}} = \alpha_{\mathrm{EKE}}\upsilon T_{40^\circ\text{–}60^\circ\mathrm{S}} - \frac{\mathrm{EKE}_{40^\circ\text{–}60^\circ\mathrm{S}}}{\tau_{\mathrm{EKE}}}, \tag{3}$$

where $\mathrm{EKE}_{40^\circ\text{–}60^\circ\mathrm{S}}$ denotes the anomalous eddy kinetic energy in the upper troposphere averaged meridionally over the band 40°–60°S, $U_{\mathrm{upper}}(\partial/\partial x)\mathrm{EKE}_{40^\circ\text{–}60^\circ\mathrm{S}}$ denotes the eastward propagation of the anomalous eddy kinetic energy by wave packets in the upper troposphere, $\alpha_{\mathrm{EKE}}\upsilon T_{40^\circ\text{–}60^\circ\mathrm{S}}$ approximates the baroclinic conversion of potential energy to eddy kinetic energy, and α_{EKE} is a linear regression coefficient. The coefficient τ_{EKE} is the damping time scale for the eddy kinetic energy.

The parameters of the model are listed in Table 1 and are found as follows.

The linear regression coefficient α_b is derived from observations by regressing zonal-mean values of anomalous $(\partial/\partial t)b_{40^\circ\text{–}60^\circ\mathrm{S}}$ onto zonal-mean values of $\upsilon T_{40^\circ\text{–}60^\circ\mathrm{S}}$, where $b_{40^\circ\text{–}60^\circ\mathrm{S}}$ is the meridional temperature gradient at 700 hPa averaged 40°–60°S and $\upsilon T_{40^\circ\text{–}60^\circ\mathrm{S}}$ is defined as the eddy fluxes of heat at 700 hPa averaged 40°–60°S. Similar results are obtained for the temperature gradient and heat fluxes at other pressure levels. The regression coefficient α_b is positive, consistent with poleward (negative) heat fluxes leading to a reduction in the baroclinicity (a decrease in the difference in temperature between 40° and 60°S).

The linear regression coefficients $\alpha_{\upsilon T}$ and α_{EKE} are derived from observations in a similar manner: $\alpha_{\upsilon T}$ is found by regressing zonal-mean values of anomalous $(\partial/\partial t)\upsilon T_{40^\circ\text{–}60^\circ\mathrm{S}}$ onto $b_{40^\circ\text{–}60^\circ\mathrm{S}}$; α_{EKE} is found by regressing zonal-mean values of anomalous $(\partial/\partial t)\mathrm{EKE}_{40^\circ\text{–}60^\circ\mathrm{S}}$ onto $\upsilon T_{40^\circ\text{–}60^\circ\mathrm{S}}$. The regression coefficient $\alpha_{\upsilon T}$ is negative, consistent with anomalously positive baroclinicity (an increase in the difference in temperature between 40° and 60°S) leading to anomalously poleward (negative) heat fluxes. The regression coefficient α_{EKE} is also negative, consistent with anomalously poleward (negative) heat fluxes leading to anomalously positive EKE.

TABLE 1. Parameters used in the simple model.

α_b	$3.7 \times 10^{-13}\,\mathrm{m^{-2}}$
$\alpha_{\upsilon T}$	$-24\,\mathrm{m^2\,s^{-2}}$
α_{EKE}	$-3 \times 10^{-5}\,\mathrm{m\,K^{-1}\,s^{-2}}$
τ_b	4 days
$\tau_{\upsilon t}$	2 days
τ_E	3 days

The linear damping coefficients are the *e*-folding time scales of the observed $\upsilon T_{40^\circ\text{–}60^\circ\mathrm{S}}$, $b_{40^\circ\text{–}60^\circ\mathrm{S}}$, and $\mathrm{EKE}_{40^\circ\text{–}60^\circ\mathrm{S}}$ time series.

The model is initiated with a Gaussian pulse in $\upsilon T_{40^\circ\text{–}60^\circ\mathrm{S}}$ centered at 0° longitude with amplitude and zonal-scale that mimics those of the observed eddy fluxes of heat at 700 hPa: the amplitude is defined as the zonal mean of the standard deviation of the eddy fluxes of heat averaged over 40°–60°S ($27\,\mathrm{K\,m\,s^{-1}}$); the Gaussian RMS width is 12° longitude.

The model is integrated with an upwind differencing scheme.

b. *Applying the simple model*

We will apply the model to three different configurations of the time-mean, zonal-mean flow: 1) no zonal advection of baroclinicity or propagation of wave activity at any level, 2) identical eastward advection of baroclinicity and propagation of wave activity in both levels, and 3) different eastward advection and propagation in the lower and upper levels. In all cases, the model is run with the parameters given in Table 1. The simulated values of zonally varying $\mathrm{EKE}_{40^\circ\text{–}60^\circ\mathrm{S}}$ are shown in Fig. 9 for all three configurations of the time-mean flow. The spectra of zonal-mean $\mathrm{EKE}_{40^\circ\text{–}60^\circ\mathrm{S}}$ and $\upsilon T_{40^\circ\text{–}60^\circ\mathrm{S}}$ are shown in Fig. 10 (the spectra of the zonal-mean circulation are identical for all three configurations of the time-mean flow).

1) CASE 1: $U_{\mathrm{lower}} = U_{\mathrm{upper}} = 0\,\mathrm{m\,s^{-1}}$

In this case, Eqs. (1) and (2) reduce to the zonally symmetric model considered in Thompson and Barnes (2014). The time series of $\upsilon T_{40^\circ\text{–}60^\circ\mathrm{S}}$ consists of a damped oscillation that—by construction—remains fixed in

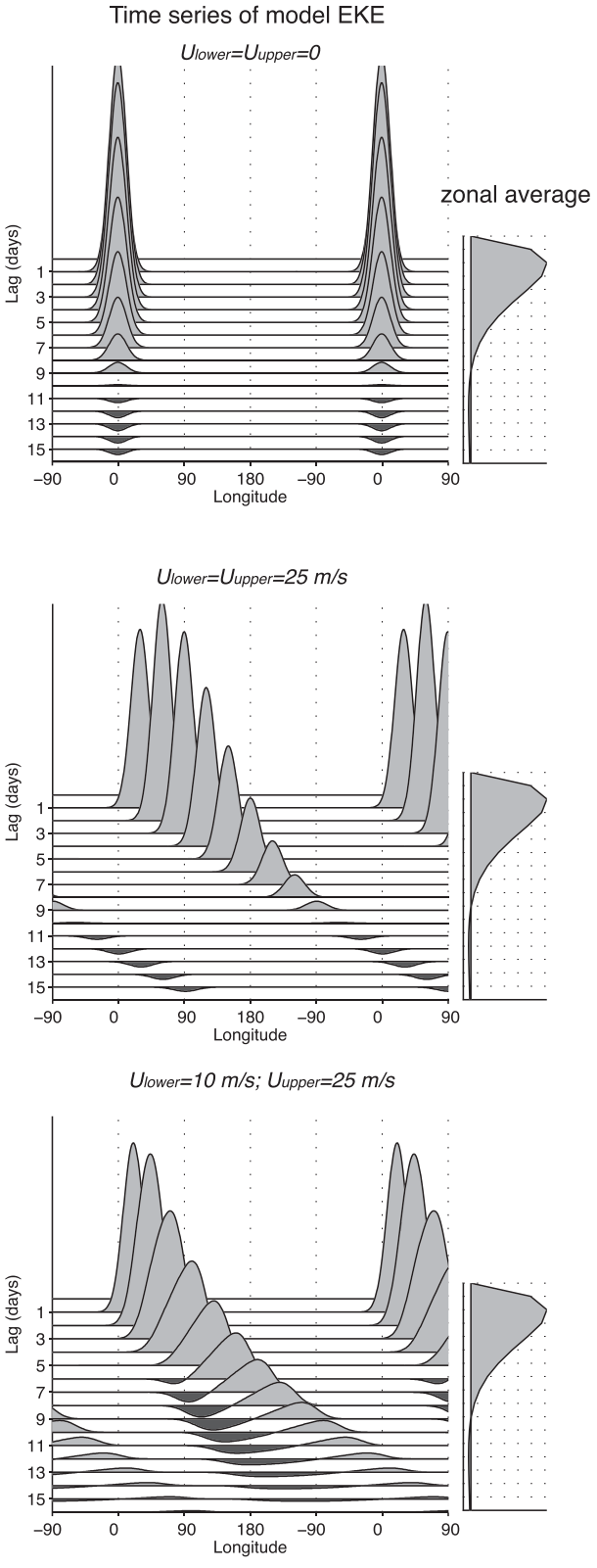

FIG. 9. Time series of EKE from the model described in section 4a. Results are shown for three different configurations of the time-mean, zonal-mean flow. (left) Results as a function of longitude; (right) zonal averages of the results. The initial amplitude of the Gaussian pulse in the eddy fluxes of heat is 27 K m s^{-1}. See text for details.

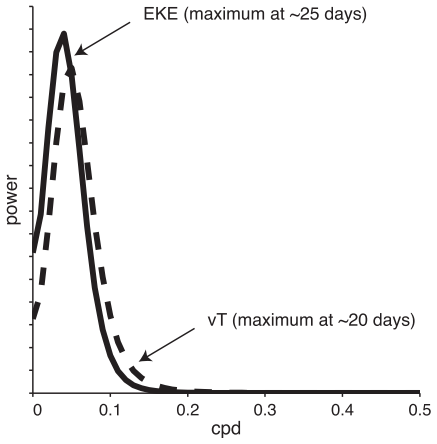

FIG. 10. Power spectra of the zonally averaged eddy kinetic energy (solid) and eddy heat fluxes (dashed) for the simulations shown in Fig. 9. The spectra are identical for all three configurations of the time-mean, zonal-mean flow. Spectra are normalized to unit variance.

longitude throughout the integration. The resulting anomalies in $\mathrm{EKE}_{40°–60°S}$ develop rapidly over the first 2 days of the integration (Fig. 9, top), decay after day 2, and reach peak negative amplitude on roughly day 14. The $\mathrm{EKE}_{40°–60°S}$ anomalies exhibit weak positive values that peak again around day 27 (results beyond day 16 are not shown).

The power spectrum of zonal-mean $vT_{40°–60°S}$ is characterized by a spectral peak centered ~20 days that is identical whether the heat fluxes are sampled at 0° longitude or are zonally averaged over all longitudes (Fig. 10, dashed line). As is the case for the observations (Fig. 8), the power spectrum of zonal-mean $\mathrm{EKE}_{40°–60°S}$ has peak amplitude at a slightly longer period than $vT_{40°–60°S}$, roughly 25 days (Fig. 10, solid line). The differences in the spectra of the simulated $\mathrm{EKE}_{40°–60°S}$ and $vT_{40°–60°S}$ time series are consistent with our parameterization of the eddy kinetic energy as a damped response to variations in the model heat fluxes [Eq. (3)]. The idealized model provides a remarkably close approximation of the simulated peaks in the eddy kinetic energy and eddy fluxes of heat despite its simplicity. The sensitivity of the periodicity in the model to variations in the model parameters is discussed in Thompson and Barnes (2014).

2) CASE 2: $U_{\mathrm{lower}} = U_{\mathrm{upper}} = 25\,\mathrm{m\,s^{-1}}$

In this case, the model baroclinicity, eddy fluxes of heat, and eddy kinetic energy are all transported eastward at a rate similar to the speed of the zonal flow in the upper troposphere, roughly 25 m s^{-1} (i.e., see Fig. 3). Conceptually, case 2 is identical to case 1, except that the model variables interact with each other along the

wave-packet path. The power spectrum of the zonal-mean model $EKE_{40°–60°S}$ and $vT_{40°–60°S}$ are identical to the power spectrum for case 1. But by construction, the damped oscillation in the model eddy kinetic energy propagates to the east at $25\,m\,s^{-1}$ (Fig. 9, middle): the Gaussian pulse again reaches peak positive amplitude on day 2 and peak negative amplitude on roughly day 14, but in this case the largest negative values occur nearly 360° to the east of the original pulse.

For both cases 1 and 2, the simulated power spectra are very similar to the observed power spectrum when the eddy fields are zonally averaged. However, neither case correctly captures the zonally varying structure of the observed eddy kinetic energy, as indicated in Figs. 4 and 5, in which opposite-signed EKE anomalies form not at a fixed longitude, nor along the path of the wave packet, but to the west of the wave packet as it propagates to the east.

3) CASE 3: $U_{lower} = 10\,m\,s^{-1}$; $U_{upper} = 25\,m\,s^{-1}$

Finally, we consider the case where 1) the eddy kinetic energy propagates to the east at a rate comparable to the speed of the zonal flow in the upper troposphere ($25\,m\,s^{-1}$) but 2) the baroclinicity is advected and heat fluxes propagate to the east at a rate comparable to the speed of the zonal flow in the lower troposphere ($10\,m\,s^{-1}$).

Applying different zonal speeds to the two levels yields results that bear strong resemblance to the zonally varying structure of the observed eddy kinetic energy (cf. Fig. 4 with Fig. 9, bottom). The Gaussian pulse in EKE again decays along the path given by $25\,m\,s^{-1}$, but in contrast to case 2, the opposite-signed anomalies in EKE form to the west of the wave packet as it propagates to the east. Conceptually, the results of case 3 can be interpreted as follows: 1) two-way interactions between the heat fluxes and baroclinicity in the lower level of the model give rise to oscillating values in $vT_{40°–60°S}$ that are transported eastward at $10\,m\,s^{-1}$ and 2) the oscillating heat fluxes drive variations in eddy kinetic energy in the upper level of the model, but the relatively fast propagation speeds in the upper troposphere ensure that successive phases of the oscillation in eddy kinetic energy appear to the west (in the wake) of the previous phase of the oscillation. As is the case for the first two configurations of the time-mean flow, the linkages between the heat fluxes and the eddy kinetic energy give rise to a slightly lower-frequency oscillation in the zonal-mean eddy kinetic energy that peaks around 20–25 days (Fig. 10).

5. Conclusions

Intraseasonal periodicity in SH wave activity is robust not only on hemispheric scales, but on regional spatial scales as well. The regional periodicity arises from out-of-phase anomalies in wave activity that form in association with extratropical wave packets as they decay and propagate to the east. At upper levels, the out-of-phase anomalies in wave activity form not along the path of decaying extratropical wave packets, but in their wake. Hence on regional scales, the periodicity in upper-tropospheric eddy kinetic energy is not apparent at a fixed location, since the opposite-signed anomalies form at a different location than the original wave packet. It is also not apparent along the eastward path of upper-tropospheric wave packets, since the opposite-signed anomalies form to the west of decaying wave packets. Rather, the periodicity in eddy kinetic energy is most clearly apparent along an eastward path that lags extratropical wave packets as they propagate to the east.

The time–longitude evolution of the periodicity in wave activity is explored in both observations and a simple two-level zonally varying model of the SH storm track. Together, the observational analyses and simple model suggest the following: 1) Intraseasonal periodicity in SH wave activity derives from feedbacks between the heat fluxes and baroclinicity in the lower troposphere. The feedbacks give rise to an oscillation in the lower-tropospheric heat fluxes on a roughly 20-day time scale that is transported to the east at a rate comparable to flow speeds in the lower troposphere ($\sim 10\,m\,s^{-1}$). 2) The heat fluxes give rise to a damped harmonic response in eddy kinetic energy that peaks on a time scale of roughly 25 days, which is slightly longer than that found in the heat fluxes. The unique time–longitude evolution of the periodicity in upper-tropospheric eddy kinetic energy is consistent with the contrasting eastward speeds of the source of the periodicity in the lower troposphere ($\sim 10\,m\,s^{-1}$) and of wave packets in the upper troposphere ($\sim 25\,m\,s^{-1}$), such that successive phases of the oscillation in eddy kinetic energy appear to the west of decaying anomalies associated with the previous phase.

The results shown here explore the origins and physics of periodicity in the SH extratropical circulation on both hemispheric and regional scales. They also reveal a novel aspect of extratropical wave packets not appreciated in previous work: that they are associated with out-of-phase anomalies in eddy kinetic energy that form to the west of decaying disturbances. The implications of the results for forecasting and surface climate will be explored in a companion study.

Acknowledgments. We thank B. J. Hoskins and an anonymous reviewer for insightful and constructive comments on the manuscript. DWJT and BRC are supported,

in part, by NSF Grant AGS-1343080. EAB is supported, in part, by NSF Grants AGS-1419818 and AGS-1545675.

REFERENCES

Ambaum, M. H. P., and L. Novak, 2014: A nonlinear oscillator describing storm track variability. *Quart. J. Roy. Meteor. Soc.*, **140**, 2680–2684, doi:10.1002/qj.2352.

Chang, E. K. M., 1993: Downstream development of baroclinic waves as inferred from regression analysis. *J. Atmos. Sci.*, **50**, 2038–2053, doi:10.1175/1520-0469(1993)050<2038:DDOBWA>2.0.CO;2.

——, 1999: Characteristics of wave packets in the upper troposphere. Part II: Hemispheric and seasonal differences. *J. Atmos. Sci.*, **56**, 1729–1747, doi:10.1175/1520-0469(1999)056<1729:COWPIT>2.0.CO;2.

——, 2005: The role of wave packets in wave–mean flow interactions during Southern Hemisphere summer. *J. Atmos. Sci.*, **62**, 2467–2483, doi:10.1175/JAS3491.1.

——, and D. B. Yu, 1999: Characteristics of wave packets in the upper troposphere. Part I: Northern Hemisphere winter. *J. Atmos. Sci.*, **56**, 1708–1728, doi:10.1175/1520-0469(1999)056<1708:COWPIT>2.0.CO;2.

Dee, D. P., and Coauthors, 2011: The ERA-Interim reanalysis: Configuration and performance of the data assimilation system. *Quart. J. Roy. Meteor. Soc.*, **137**, 553–597, doi:10.1002/qj.828.

Feldstein, S. B., 2003: The dynamics of NAO teleconnection pattern growth and decay. *Quart. J. Roy. Meteor. Soc.*, **129**, 901–924, doi:10.1256/qj.02.76.

Hartmann, D. L., and F. Lo, 1998: Wave-driven zonal flow vacillation in the Southern Hemisphere. *J. Atmos. Sci.*, **55**, 1303–1315, doi:10.1175/1520-0469(1998)055<1303:WDZFVI>2.0.CO;2.

Hoskins, B. J., and P. J. Valdes, 1990: On the existence of storm tracks. *J. Atmos. Sci.*, **47**, 1854–1864, doi:10.1175/1520-0469(1990)047<1854:OTEOST>2.0.CO;2.

Kidson, J. W., 1988: Interannual variations in the Southern Hemisphere circulation. *J. Climate*, **1**, 1177–1198, doi:10.1175/1520-0442(1988)001<1177:IVITSH>2.0.CO;2.

Lee, S., and I. M. Held, 1993: Baroclinic wave packets in models and observations. *J. Atmos. Sci.*, **50**, 1413–1428, doi:10.1175/1520-0469(1993)050<1413:BWPIMA>2.0.CO;2.

Li, Y., and D. W. J. Thompson, 2016: Observed signatures of the barotropic and baroclinic annular modes in cloud vertical structure and cloud radiative effects. *J. Climate*, **29**, 4723–4740, doi:10.1175/JCLI-D-15-0692.1.

Lindzen, R. S., and B. F. Farrell, 1980: A simple approximate result for the maximum growth rate of baroclinic instabilities. *J. Atmos. Sci.*, **37**, 1648–1654, doi:10.1175/1520-0469(1980)037<1648:ASARFT>2.0.CO;2.

Novak, L., M. H. P. Ambaum, and R. Tailleux, 2015: The lifecycle of the North Atlantic storm track. *J. Atmos. Sci.*, **72**, 821–833, doi:10.1175/JAS-D-14-0082.1.

Rossby, C.-G., and H. C. Willett, 1948: The circulation of the upper troposphere and lower stratosphere. *Science*, **108**, 643–652, doi:10.1126/science.108.2815.643.

Simmons, A. J., and B. J. Hoskins, 1978: The life cycles of some nonlinear baroclinic waves. *J. Atmos. Sci.*, **35**, 414–432, doi:10.1175/1520-0469(1978)035<0414:TLCOSN>2.0.CO;2.

——, and ——, 1979: The downstream and upstream development of unstable baroclinic waves. *J. Atmos. Sci.*, **36**, 1239–1254, doi:10.1175/1520-0469(1979)036<1239:TDAUDO>2.0.CO;2.

Thompson, D. W. J., and J. M. Wallace, 2000: Annular modes in the extratropical circulation. Part I: Month-to-month variability. *J. Climate*, **13**, 1000–1016, doi:10.1175/1520-0442(2000)013<1000:AMITEC>2.0.CO;2.

——, and E. A. Barnes, 2014: Periodic variability in the large-scale Southern Hemispheric circulation. *Science*, **343**, 641–645, doi:10.1126/science.1247660.

——, and J. D. Woodworth, 2014: Barotropic and baroclinic annular variability in the Southern Hemisphere. *J. Atmos. Sci.*, **71**, 1480–1493, doi:10.1175/JAS-D-13-0185.1.